Li *et al. Microstructures* **2025**, *5*, 2025008
DOI: 10.20517/microstructures.2024.78

Microstructures

Research Article

Open Access

High-pressure modulation of band gap and microstructure in N-type high-entropy strontium titanate for enhanced thermoelectric performance

Xinjian Li[1,2,3], Xiaohuan Luo[1], Moran Wang[1], Tu Lyu[1], Chaohua Zhang[1], Fusheng Liu[1], Hongan Ma[3], Lipeng Hu[1]

[1]College of Materials Science and Engineering, Shenzhen Key Laboratory of Special Functional Materials, Guangdong Research Center for Interfacial Engineering of Functional Materials, Guangdong Provincial Key Laboratory of Deep Earth Sciences and Geothermal Energy Exploitation and Utilization, Institute of Deep Earth Sciences and Green Energy, Shenzhen University, Shenzhen 518060, China
[2]College of Physics and Optoelectronic Engineering, Shenzhen University, Shenzhen 518060, China
[3]State Key Laboratory of Superhard Materials, College of Physics, Jilin University, Changchun 130012, Jilin, China

Correspondence to: Prof. Hongan Ma, State Key Laboratory of Superhard Materials, College of Physics, Jilin University, 2699 Qianjin St., Changchun 130012, Jilin, China. E-mail: maha@jlu.edu.cn; Dr. Lipeng Hu, College of Materials Science and Engineering, Shenzhen Key Laboratory of Special Functional Materials, Guangdong Research Center for Interfacial Engineering of Functional Materials, Guangdong Provincial Key Laboratory of Deep Earth Sciences and Geothermal Energy Exploitation and Utilization, Institute of Deep Earth Sciences and Green Energy, Shenzhen University, Building 1066, Xueyuan Avenue, Nanshan District, Shenzhen 518060, China. E-mail: hulipeng@szu.edu.cn

How to cite this article: Li, X.; Luo, X.; Wang, M.; Lyu, T.; Zhang, C.; Liu, F.; Ma, H.; Hu, L. High-pressure modulation of band gap and microstructure in N-type high-entropy strontium titanate for enhanced thermoelectric performance. *Microstructures* **2025**, *5*, 2025008. https://dx.doi.org/10.20517/microstructures.2024.78

Received: 29 Aug 2024 **First Decision:** 14 Oct 2024 **Revised:** 22 Oct 2024 **Accepted:** 21 Nov 2024 **Published:** 23 Jan 2025

Academic Editors: Jing-Feng Li, Li-Dong Zhao, Zhigang Chen **Copy Editor:** Ping Zhang **Production Editor:** Ping Zhang

Abstract

In thermoelectrics, optimizing both carrier and phonon transport is crucial for enhancing thermoelectric performance. Strontium titanate, a representative N-type oxide thermoelectric material, often exhibits inferior figure of merit (zT) due to its large band gap that limits carrier concentration, and high lattice thermal conductivity, attributed to strong Ti-O covalent bonds. Conventional approaches, such as aliovalent doping to increase carrier concentration or introducing structural defects to reduce lattice thermal conductivity, are insufficient as they fail to decouple the interdependent electrical and thermal properties. Herein, we introduce a high-pressure synthesis technique that concurrently modulates both the band gap and microstructure. This approach effectively enhances the carrier concentration by narrowing the band gap and increases the effective mass of the density of states through enhanced solubility limit of rare earth elements, significantly improving the power factor. Additionally, high-pressure condition induces microstructural defects, including point defects, dislocations, lattice distortions,

and nanoscale grains, which promote broad-wavelength phonon scattering and minimize lattice thermal conductivity. Consequently, a peak zT value of 0.25 at 973 K is attained in high-entropy $(Sr_{0.2}La_{0.2}Nd_{0.2}Sm_{0.2}Eu_{0.2})TiO_3$ synthesized at 5 GPa, representing a 5.3-fold improvement over undoped strontium titanate. This work highlights the pivotal role of high-pressure synthesis in decoupling the carrier and phonon transport in thermoelectrics.

Keywords: Thermoelectric, strontium titanate, high pressure, band gap, microstructure

INTRODUCTION

Thermoelectric (TE) materials, endowed with the ability to directly convert heat into electricity and vice versa, provide a promising solution to the global energy crisis and environmental pollution[1-3]. The performance of TE materials is quantified by the dimensionless figure of merit (zT), as determined by $zT=\sigma\alpha^2T/\kappa$, where σ, α, κ and T represent the electrical conductivity, the Seebeck coefficient, the total thermal conductivity (κ), and the absolute temperature, respectively[4]. Achieving an optimal zT requires a delicate balance of properties that are inherently conflicting: high σ reminiscent of metals, large α characteristic of ceramics, and low κ akin to glasses[5]. Nevertheless, the intricate coupling among these physical parameters complicates the concurrent optimization of carrier and phonon transport, which remains a pivotal barrier to improving TE performance.

To date, chalcogenides, encompassing V_2VI_3 and IV-VI compounds, have emerged as prominent candidates for solid-state refrigeration and power generation across low- and medium-temperature applications[6-11]. Despite their significant potential, these materials face limitations due to toxicity, susceptibility to oxidation, and high production costs, which curtail their widespread practical deployment. Besides, chalcogenides with exceptional zT values often feature metavalent bonding[12-15]. This bonding involves half-filled σ-bonds formed by perpendicular p-orbitals, allowing the sharing of approximately one electron between adjacent atoms[13,14]. This unique bonding configuration endows the material with a certain softness and extreme brittleness, thereby increasing manufacturing expenses and reducing the longevity essential for reliable TE device operation.

To confront these challenges, oxide TE materials have gained prominence due to their exceptional thermal stability, corrosion resistance, non-toxicity, inexpensive, and robust mechanical properties, positioning them as ideal candidates for high-temperature TE applications[16]. While numerous P-type oxides, such as BiCuSeO[17], $Ca_3Co_4O_9$[18], and $NaCo_2O_4$[19], consistently demonstrate a zT value exceeding 1.0, N-type oxides, in contrast, generally achieve lower zT values, typically ranging from 0.1 to 0.5[20,21]. Theoretical calculation suggests that strontium titanate ($SrTiO_3$) holds potential as a promising N-type oxide TE material with a potential zT of 0.7[22]. Nonetheless, experimental studies reveal that the zT of $SrTiO_3$-based materials typically approximates 0.2[23,24], with only isolated reports of higher values[25]. This performance limitation can be primarily ascribed to its intrinsically high lattice κ (κ_L) stemming from the strong Ti-O covalent bond, with single-crystal $SrTiO_3$ demonstrating a κ_L of 12 $Wm^{-1}K^{-1}$ at 300 K[26]. Additionally, the exceptionally low carrier concentration (n_H) in pristine $SrTiO_3$, with values about 10^{18} cm^{-3}, leads to less-than-ideal zT of 0.047 stemming from its wide band gap (E_g) of 3.2 eV[27-29]. Thus, effectively balancing the reduction of κ_L while enhancing σ is crucial for optimizing the TE performance of $SrTiO_3$ and other N-type oxide materials.

Owing to intrinsic oxygen vacancy defects, pristine $SrTiO_3$ exhibits N-type conductivity. Efforts to enhance the TE performance of $SrTiO_3$ have focused on increasing n_H by either amplifying oxygen vacancies or

implementing aliovalent doping. In the ABO_3 perovskite structure of $SrTiO_3$, prevalent doping strategies include substituting La at the A-site[30], or Nb at the B-site[31], and co-doping at both sites[25] to optimize the n_H and subsequently improve the electrical transport properties. While conventional doping can elevate the n_H to approximately 10^{19} cm^{-3}[32], achieving the theoretical optimum n_H of 3~4 × 10^{20} cm^{-3}[22] continues to be a challenge. In addition, strategies to lower the κ_L typically involve the intricate design and modulation of microstructures at multiple scales, such as introducing point defects, creating grain boundaries, and engineering superlattices and nanostructures to scatter broad-wavelength phonons[33,34]. Despite these efforts, the reported minimum κ_L of $SrTiO_3$-based materials persistently exceeds 3 $Wm^{-1}K^{-1}$[35,36]. Furthermore, the introduction of these microstructures, often achieved through various methods, presents significant challenges in terms of integration and control. Therefore, there is a pressing need for an innovative strategy that allows for the coordinated optimization of both carrier and phonon transport in $SrTiO_3$-based materials by concurrently tailoring both their band structures and microstructures.

Pressure, a fundamental thermodynamic parameter, finds applications across numerous disciplines. For instance, high-pressure environments are crucial in synthesizing diamonds and superhard materials[37,38], enabling photoluminescence in metal halide perovskites[39], and generating novel substances such as amorphous carbon under extreme conditions[40]. With the increasing application of high-pressure technology, its use has also been reported in alloy-based TE materials[41]. High-pressure synthesis (≥ 1 GPa) constitutes a pivotal and innovative approach for precisely manipulating the electronic band structure and microstructure[42]. Despite the preservation of structural and stoichiometric integrity under high pressure, the electronic properties may undergo significant alterations. The application of physical pressure reduces interatomic distances and enhances interatomic interactions, which results in the modulation of band structure[43]. For example, the band overlap driven by high pressure can induce transition, such as from an insulator to a metal or from a semiconductor to a metal[42]. In this context, the tuning of TE parameters by applied pressure can be likened to the optimization of n_H by a pressure-tuned E_g. Besides, the driving force generated by high pressure significantly alters the reaction equilibrium, thereby facilitating the incorporation of dopants beyond the solubility limit into the matrix and introducing dense point defects[44]. Concurrently, the compression of atomic spacing under high pressure intensifies localized stress within the material, potentially leading to the formation of high-density dislocations[45]. Additionally, the compression of atomic distances often causes deviations from ideal atomic positions within the crystal lattice, thereby resulting in lattice distortions[46]. Lastly, such stress also promotes the fracturing and deformation of large grains and constrains grain growth, which contributes to the formation of nanograins[46]. Therefore, the microstructures engineered under high pressure, comprising point defects, dislocations, lattice distortions and nanoscale grains, substantially enhance phonon scattering and effectively restrain the κ_L. While several oxide materials prepared under high pressure, including non-stoichiometric titanium oxide, ZnO, and BiCuSeO, have demonstrated promising zT values[47-49], there remains a notable absence of reports on the high-pressure synthesis of $SrTiO_3$-based TE materials.

In this work, we leveraged high-pressure synthesis to strategically manipulate both the band structure and microstructure of high-entropy $(Sr_{0.2}La_{0.2}Nd_{0.2}Sm_{0.2}Eu_{0.2})TiO_3$ materials, with the explicit aim of achieving the maximal reduction in κ_L. The use of $SrTiO_3$-based high-entropy materials in TE applications has been documented in previous studies[32,50]. However, the reported doping elements are typically isovalent, with ion radii comparable to that of the host matrix. In contrast, the doping elements employed in this research are heterovalent, and their ion radii differ from those of the matrix. High pressure facilitates the formation of a single-phase solid solution, surpassing the conventional doping tolerance limit typically observed under standard atmospheric conditions. Additionally, it reduces the E_g, which elevates the n_H and consequently enhances the power factor (PF). Simultaneously, the application of high pressure induces dense point

defects, dislocations, lattice distortions and nanoscale grains, all of which are instrumental in promoting broad-frequency phonon scattering. The multiscale microstructures developed under a pressure of 5 GPa significantly reduced the κ_L to 0.8 $Wm^{-1}K^{-1}$ at 973 K, a figure notably lower than most reported in the existing literature. Consequently, a peak zT of 0.25 at 973 K was recorded for the sample synthesized under 5 GPa; this represents a 5.3-fold enhancement over the original $SrTiO_3$ sample synthesized under standard atmospheric conditions[28]. This work highlights the potential of high-pressure synthesis to manipulate the E_g and microstructure, offering a promising pathway for the advancement of TE materials.

EXPERIMENTAL PROCEDURES

Synthesis recipe

The high-entropy $(Sr_{0.2}La_{0.2}Nd_{0.2}Sm_{0.2}Eu_{0.2})TiO_3$ samples were synthesized through a standard high temperature and high pressure (HPHT) solid-state reaction. Reagents including SrO, La_2O_3, Nd_2O_3, Sm_2O_3, Eu_2O_3, TiO_2 (AR), and extra Ti, each with a purity of 99.99%, were purchased from Aladdin. These reagents were accurately weighed to ensure stoichiometric precision with an error margin below 0.0001 g. The mixture was uniformly blended using an agate mortar and pestle. The resultant powder was cold-pressed into a cylinder, measuring 10.5 mm in diameter and 6 mm in thickness, and encased in molybdenum foil to prevent contamination. The samples were then sintered under HPHT conditions at 1073 K for 40 min using a Chinese hexagonal anvil high-pressure device (CHPA SPD-6×1200), with pressure of 3, 4, and 5 GPa, as illustrated in Figure 1A. Thereafter, these samples have been designated as 3 GPa, 4 GPa, and 5 GPa, respectively. Temperature uniformity was ensured by an electrified graphite ring, while pressure was applied via a hydraulic multi-anvil instrument. Temperature and pressure were calibrated with a B-type platinum-rhodium thermocouple and standard phase transition point, respectively. After synthesis, the obtained samples underwent rapid quenching under high pressure to ensure solidification.

Phase and microstructure characterization

The phase structure and crystallinity of the samples were analyzed through X-ray diffraction (XRD, Rigaku d/Max 2550 V/PC, Japan), employing Cu-Kα Radiation (λ = 0.15418 nm) over a 2θ range of 20-80°. To quantify the impact of pressure on the crystal structure of samples, we utilized the Fullprof Suite for structure refinement, analyzing the lattice parameters across the samples. The fracture surface morphology was observed with field emission scanning electron microscopy (SEM) using a JEOL JSM-6700F. High-resolution transmission electron microscopy (HRTEM), conducted with a JEOL JEM-2200FS, provided detailed insights into the microstructures. The E_g was assessed using a UV-3150 double-beam spectrophotometer.

Transport property measurements

The sintered samples had a diameter of 10 mm and a thickness of around 4 mm. Initial surface polishing was conducted using fine-grit sandpaper, followed by sectioning the sample into two 2 mm slices using a wire cutter (STX-202A, China).

The σ and α were measured using a Namicro-□ L TE testing system. The thermal diffusion coefficient (D) was evaluated via a laser flash method (Netzsch LFA 467, Germany). The κ was calculated using: $\kappa = DC_p\rho$, where the heat capacity (C_p) was estimated based on the Dulong-Petit law, and sample density (ρ) was determined following Archimedes' principle with an electronic balance (AE124J). The room-temperature n_H and carrier mobility (μ_H) were calculated from $n_H = 1/eR_H$ and $\mu_H = \sigma R_H$, respectively. Here, the Hall coefficient (R_H) was measured using a Physical Property Measurement System (PPMS-9, Quantum Design®, USA).

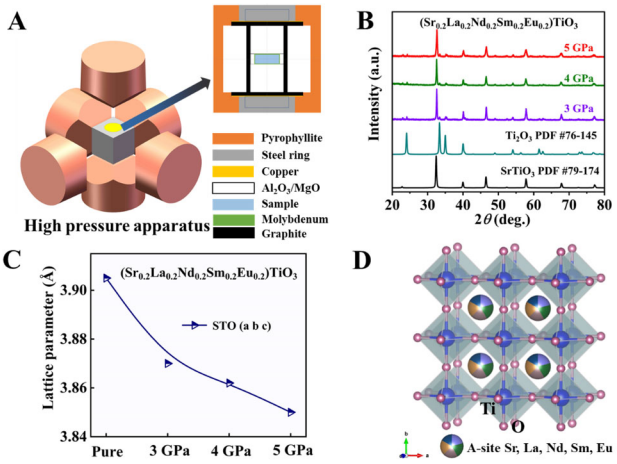

Figure 1. (A) Schematic diagram of HPHT synthesis process; (B) X-ray diffraction (XRD) patterns of $(Sr_{0.2}La_{0.2}Nd_{0.2}Sm_{0.2}Eu_{0.2})TiO_3$ synthesized under varying pressures; (C) Lattice parameters calculated by Rietveld refinement; (D) Schematic representation of the high-entropy $SrTiO_3$ crystal structure. HPHT: High temperature and high pressure.

RESULTS AND DISCUSSION

Figure 1B illustrates the XRD patterns of high-entropy $(Sr_{0.2}La_{0.2}Nd_{0.2}Sm_{0.2}Eu_{0.2})TiO_3$ ceramics with added excess Ti powder. The primary goal of incorporating additional Ti is to establish a reducing environment that fosters the formation of oxygen vacancies, thereby increasing the n_H. The surplus Ti reacts with oxygen to produce non-stoichiometric titanium oxide, effectively circumventing the gradient distribution of oxygen vacancies typically associated with conventional short-term reduction annealing. Unlike previous methods that use atmospheric pressure and doped Ti powder, which generally result in TiO_2 remaining as a discrete phase within the matrix[51,52], this work underscores the distinctive advantage of the HPHT synthesis method, which facilitates the chemical reaction unachievable under normal atmospheric conditions.

We analyzed the XRD data for the samples prepared under 3, 4, and 5 GPa via the Rietveld refinement method [Supplementary Figure 1]. The lattice parameters, as refined from the XRD data and depicted in Figure 1C, demonstrate a notable reduction in the lattice parameter of high-entropy $(Sr_{0.2}La_{0.2}Nd_{0.2}Sm_{0.2}Eu_{0.2})TiO_3$ with increasing synthesis pressure. This reduction indicates that high-pressure condition compresses the atomic spacing, thereby significantly altering the band structure and electronic properties of the high-entropy $(Sr_{0.2}La_{0.2}Nd_{0.2}Sm_{0.2}Eu_{0.2})TiO_3$ ceramics.

From a crystallographic perspective, the perovskite structure is versatile in its ability to host various ions at lattice points, thereby facilitating the formation of a single-phase solid solution. The structural stability of perovskite oxides is typically assessed using Goldschmidt's tolerance coefficient (t), a critical metric in determining lattice compatibility and overall stability[53]. In order to determine the structural stability of high-entropy $(Sr_{0.2}La_{0.2}Nd_{0.2}Sm_{0.2}Eu_{0.2})TiO_3$, we examined its t, as defined by[53]:

$$t = \frac{r_A + r_O}{\sqrt{2}(r_B + r_O)} = \frac{\left(\frac{r_{Sr} + r_{La} + r_{Nd} + r_{Sm} + r_{Eu}}{5}\right) + r_o}{\sqrt{2}(r_{Ti} + r_O)} \quad (1)$$

where r_A, r_B, r_{Sr}, r_{La}, r_{Nd}, r_{Sm}, r_{Eu}, r_{Ti}, and r_O are the ionic radii of cations A, B, Ti, Sr, La, Nd, Sm, Eu, Ti and anion O, respectively. Details regarding the valence states and ionic radii of these elements are provided in Supplementary Table 1. The structural implications of the t are profound: t less than 0.9 typically indicates a propensity for forming orthorhombic or rhombohedral phase; t between 0.9 and 1 suggests a likelihood of a stable cubic phase; t greater than 1 often leads to tetragonal or hexagonal phase. The calculated t of our

high-pressure synthesized $(Sr_{0.2}La_{0.2}Nd_{0.2}Sm_{0.2}Eu_{0.2})TiO_3$ material is 0.854, which traditionally would not favor a stable cubic phase structure. Despite this, the high-pressure synthesis significantly alters the dynamics within the crystal structure[54]. The intense pressure increases the solubility limits for dopants and drives more elements into the lattice[44], thereby increasing the system's configurational entropy, and achieving a highly symmetrical cubic structure despite the lower *t*. The crystal structure diagram is shown in Figure 1D. This phenomenon not only underscores the critical role of high pressure in expanding the solubility limit of dopants and stabilizing the structure but also in inducing dense point defects, which significantly scatter high-frequency phonons.

The microstructure plays a crucial role in determining the electrical and thermal transport, ultimately affecting the zT value[3]. Supplementary Figure 2 presents the SEM image of the samples, revealing micron-sized grains and a clearly dense morphology. This observation indicates that the samples synthesized under high pressure exhibit excellent compactness. To investigate the impact of high pressure on the microstructure, we performed transmission electron microscopy (TEM) analysis on a sample synthesized under 5 GPa, with the results presented in Figure 2. Figure 2A displays a low-resolution image, revealing the presence of nanoscale grains ranging from 20 nm to 100 nm in size that are separated by clear boundaries. This underscores the capability of high pressure to refine certain grains under high-temperature synthesis conditions. Such grain refinement results in an increased number of grain boundaries, which serve as effective phonon scattering centers and thus decrease the κ_L[55]. In addition, a combination of microstructural characterization and volumetric density measurement indicates a high-density sample, which is conducive to maintaining decent μ_H. Therefore, the HPHT synthesis method exhibits superior efficacy in synergistically optimizing the electron and phonon transport properties compared to conventional synthesis means.

The HRTEM image [Figure 2B] demonstrates a well-defined atomic arrangement, with the corresponding fast Fourier transformation (FFT) analysis (inset) confirming a cubic phase view along the [001] direction. Figure 2C presents a zoomed-in view of the atomic arrangement image taken from Figure 2B, which matches well with the crystal structure model of cubic $SrTiO_3$. Figure 2D, captured in dark-field image mode complemented by energy dispersive spectrum (EDS) elemental mapping, demonstrates that all elements are evenly distributed [Supplementary Figures 3 and 4], with some elements visibly enriched at the grain boundaries. Figure 2E and F further illustrates a close-up of these element-enriched regions, revealing a concentration of brighter atoms at the grain boundaries. This may be attributed to the differential ion migration rate under high pressure, where the dopants are more readily captured by the high-energy interfaces, thereby forming the barriers to inhibit grain growth[56]. Additionally, the enrichment of multi-atoms at grain boundaries significantly enhances the phonon scattering, further diminishing the κ_L[57,58].

The micromorphology depicted in Figure 2G illustrates the regularly distributed lattice distortions. To delve deeper into these lattice defects, the inverse FFT (IFFT) analysis was performed, revealing clearly observable edge dislocations, as presented in Figure 2H and Supplementary Figure 4. These distortions and edge dislocations may originate from the large strain introduced during the HPHT process[59], and imperfect atom arrangement due to multiple atoms occupying Sr sites. The stain field distribution surrounding these distortions and dislocations, characterized in Figure 2G, was analyzed using geometric phase analysis (GPA). The results, as displayed in Figure 2I-L, show a pronounced presence of compressive (blue) and tensile (red) stresses, with a notable strain gradient evident near the interface between perfect lattice regions and defects-rich areas. The high-strain arrays confirm the presence of highly distorted microstructures. The cumulative effect of chemical stress from multi-element doping and the physical stress induced by high

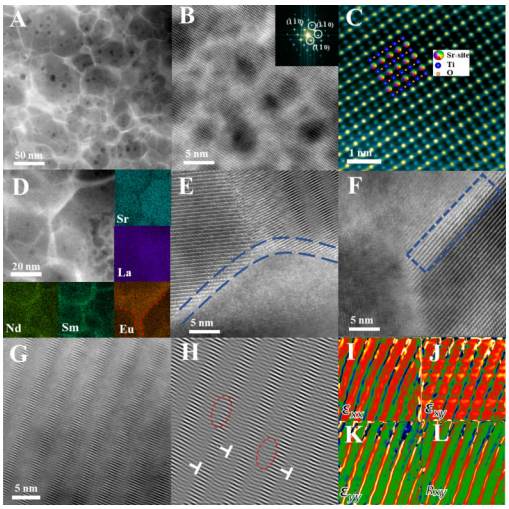

Figure 2. Structural characterizations of the 5 GPa sample using transmission electron microscopy (TEM); (A) Low-resolution TEM image showing the clear grain boundaries; (B) High-resolution TEM (HRTEM) image and fast Fourier transformation (FFT) analysis (inset) indicating a cubic phase view along the [001] direction; (C) A close-up view of atomic arrangement with corresponding atomic model of cubic $SrTiO_3$; (D) TEM image and energy dispersive spectrum (EDS) mapping of the elements Sr, La, Eu, Sm, Nd, revealing the dopants are concentrated at the grain boundary; (E and F) High-magnification images of the grain boundary, with brightness variations indicating elemental enrichment; (G) HRTEM image and (H) inverse fast Fourier transformation (IFFT) analysis illustrating lattice distortions and edge dislocations; (I-L) Corresponding strain maps of Figure 2(C) analyzed by geometric phase analysis (GPA) method.

pressure leads to a pronounced strain distribution[60]. This concomitant strain field fluctuation serves as an effective impediment to phonon transport. This intricate interplay of stress not only demonstrates the complex nature of material responses under HPHT conditions but also underscores the potential for tailored microstructural engineering to optimize TE performance.

To elucidate the impact of high-pressure synthesis on the electrical properties of $(Sr_{0.2}La_{0.2}Nd_{0.2}Sm_{0.2}Eu_{0.2})TiO_3$ ceramics, we measured the n_H and μ_H at room temperature, as illustrated in Figure 3A. In stark contrast to pristine $SrTiO_3$, which exhibits a notably low n_H = 1.1 × 10^{18} cm^{-3} under atmospheric pressure[28], our high-pressure synthesis achieves an impressive n_H of up to 10^{20} cm^{-3}. Moreover, the application of physical pressure leads to a progressive rise in n_H, which is likely attributed to pressure-induced modifications in the band structure. Specifically, the room-temperature n_H rises from 2.1 × 10^{20} cm^{-3} for the 3 GPa sample to 2.7 × 10^{20} cm^{-3} for the 4 GPa sample, and further to 4.3 × 10^{20} cm^{-3} for the 5 GPa sample, representing approximately a two-fold enhancement. Given the complex chemical compositions and the challenges associated with high-pressure conditions, direct theoretical calculation of the band structure is difficult. Therefore, we conducted optical measurement of E_g, as presented in Figure 3B. The result reveals a decrease in E_g with increasing pressure. High-pressure synthesis compresses the interatomic distance and enhances the orbital coupling, leading to a narrowing of E_g [42,44]. Concurrently, various rare earth elements were successfully incorporated into the $SrTiO_3$ lattice under high pressure. Dopants such as La, Sm and Eu, with their unique incomplete 4f orbitals and vacant 5d orbitals, enable 4f electrons to jump between f-f or f-d configurations. This process introduces impurity levels into the forbidden band, further narrowing the E_g [61]. To the best of our knowledge, this represents one of the highest reported n_H for N-type $SrTiO_3$ materials, approaching the theoretical optimal value for such materials.

The implementation of high pressure introduces intricate microstructures that can scatter carriers, while also narrowing the E_g, which enhances the carrier-carrier scattering. Despite these adverse effects, the μ_H at room temperature exhibits only a marginal decline with increasing pressure. For instance, μ_H drops

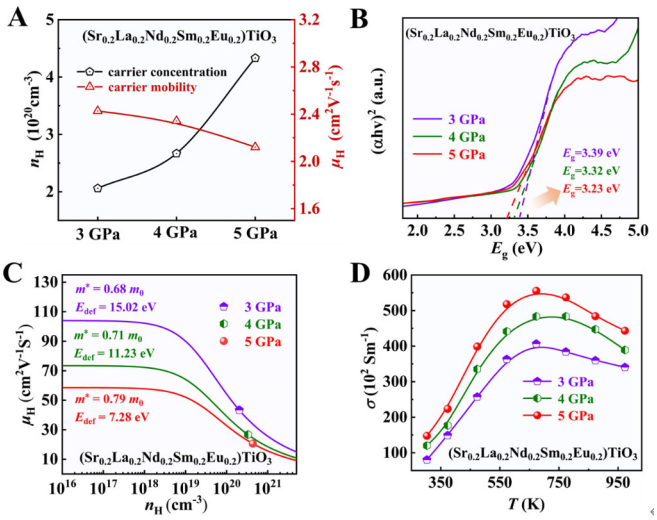

Figure 3. (A) Room-temperature carrier concentration (n_H) and carrier mobility (μ_H) of the 3 GPa, 4 GPa, and 5 GPa samples; (B) Optical band gap determined by UV spectroscopy; (C) The calculated μ_H *versus* n_H curves based on the SPB model; (D) Temperature dependence of electrical conductivity (σ) for the 3 GPa, 4 GPa, and 5 GPa samples. SPB: Single parabolic band.

modestly from 2.4 $cm^2V^{-1}s^{-1}$ for 3 GPa sample to 2.3 $cm^2V^{-1}s^{-1}$ for 4 GPa sample, and subsequently to 2.1 $cm^2V^{-1}s^{-1}$ for 5 GPa sample. This phenomenon raises a pertinent question: Why does high pressure exert such a limited detrimental effect on the μ_H in high-entropy $(Sr_{0.2}La_{0.2}Nd_{0.2}Sm_{0.2}Eu_{0.2})TiO_3$? One plausible explanation is that the inherently low μ_H in this high-entropy system constrains the carrier mean-free path near the Mott-Ioffe-Regel limit[62,63]. Consequently, physical pressure has a negligible impact on further reducing μ_H. Additionally, aside from the commonly considered defect-carrier scattering and carrier-carrier scattering mechanisms, the role of acoustic phonons scattering, quantified by the deformation potential E_{def}, is also crucial[3]. We have evaluated the E_{def} by analyzing the n_H versus μ_H curves using the single parabolic band (SPB) model[64] [Figure 3C]. Apparently, the result discloses a pronounced decline in E_{def} with rising synthesis pressure, from a value of 15.0 eV for the 3 GPa sample to 7.3 eV for the 5 GPa sample. This substantial diminution in E_{def} indicates mitigated acoustic phonon scattering, which helps maintain a relatively decent μ_H under high pressure. Moreover, it is noteworthy that the E_{def} for $(Sr_{0.2}La_{0.2}Nd_{0.2}Sm_{0.2}Eu_{0.2})TiO_3$ under high-pressure conditions is significantly lower than values observed in traditional high-performance TE materials such as PbTe and Bi_2Te_3, and is on par with those found in newly studied heavy-effective-mass systems such as ZrNiSn, FeNbSb, and MgAgSb[3]. The underlying mechanisms by which high pressure leads to such a reduction in E_{def} warrant further exploration in future research endeavors.

Figure 3D shows the σ as a function of temperature under varying synthesis pressures. Firstly, it exhibits an increase followed by a decrease with rising temperature, signifying a transition in the electrical transport mechanism from semiconductor-like at lower temperatures to metal-like conductivity at higher temperatures. Besides, the σ progressively increases with heightened synthesis pressure, attributed to a large elevation in n_H, despite a marginal reduction in μ_H. For instance, the σ at room temperature rises markedly from 80.3 Scm^{-1} for the 3 GPa sample to 147.7 Scm^{-1} for the 5 GPa sample.

As depicted in Figure 4A, the α of all samples is negative, and its absolute value increases monotonously with temperature, confirming that all $(Sr_{0.2}La_{0.2}Nd_{0.2}Sm_{0.2}Eu_{0.2})TiO_3$ samples behave as N-type degenerate semiconductors. The magnitude of α is principally influenced by the n_H and the density-of-states effective mass (m^*)[65]. In a degenerate semiconductor, α can be quantitatively expressed using the Mott equation

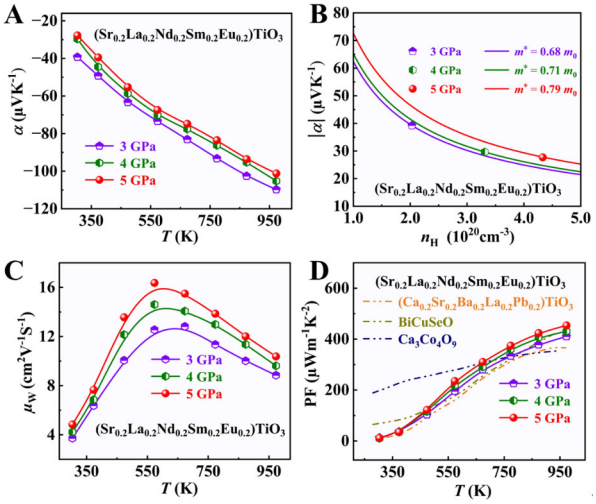

Figure 4. (A) Temperature dependence of Seebeck coefficient (α) for the 3 GPa, 4 GPa, and 5 GPa samples; (B) Room temperature Pisarenko plots calculated using the SPB model; (C) The calculated temperature-dependent weight mobility μ_W of the 3 GPa, 4 GPa, and 5 GPa samples; (D) Power factor (PF) as a function of temperature for the 3 GPa, 4 GPa, and 5 GPa samples, the literature data are also shown for comparison[68-70].

derived from the SPB model, as given in[7]:

$$\alpha = \frac{8\pi^2 k_B^2}{3eh^2} m^* T \left(\frac{\pi}{3n_H}\right)^{\frac{2}{3}} \quad (2)$$

where e is the electron charge, h represents the Planck constant, and k_B refers to the Boltzmann constant. Despite the substantial increase in n_H, α only exhibits a slight reduction with increasing physical pressure. To further elucidate this behavior, we computed the Pisarenko curves to estimate the m^* of all samples at room temperature employing the SPB model[64], as plotted in Figure 4B. Typically, the m^* shows a gradual increase from 0.68 m_0 for the 3 GPa sample to 0.79 m_0 for the 5 GPa sample. The rare earth elements, with their 4f orbitals and localized magnetic moments, substantially contribute to a high m^*[66], a feature enhanced by high-pressure sintering, which effectively incorporates these rare earth elements into the matrix. Consequently, the elevated m^* sustains a robust α even with high n_H. Typically, at room temperature, α marginally reduces from -39.2 μVK^{-1} for the 3 GPa sample to -27.7 μVK^{-1} for the 5 GPa sample, illustrating a balanced interplay between increased n_H and m^* under varying pressure conditions.

Under the premise of achieving optimal n_H, the electronic transport properties can be quantitatively evaluated by the weighted mobility $\mu_W = \mu_H m^{*3/2}$[67]. As depicted in Figure 4C, the μ_W displays a notable increase with higher synthetic pressure, indicating that high synthesis pressure is effective in enhancing electronic transport properties. This improvement is further substantiated by the calculated PF presented in Figure 4D, where the PF exhibits a moderate increase with elevating physical pressure. This increment in PF is primarily attributed to the elevated σ, notwithstanding the minor reduction in the α. Interestingly, the PF continues to ascend without showing signs of saturation, even at elevated temperatures, suggesting that further enhancement in PF at higher temperatures is feasible. Specifically, the PF at 973 K increases from 410 μWm^{-1}K^{-2} to 453 μWm^{-1}K^{-2} (10% enhancement). This improvement is achieved by modifying the synthesis conditions without altering sample composition, further highlighting the advantages of high-pressure optimization of material properties. Compared with previously documented data on P-type BiCuSeO, $Ca_3Co_4O_9$ and high-entropy alloyed $SrTiO_3$ ceramics[68-70], the PF achieved under high-pressure synthesis conditions is notably superior, especially at elevated temperatures.

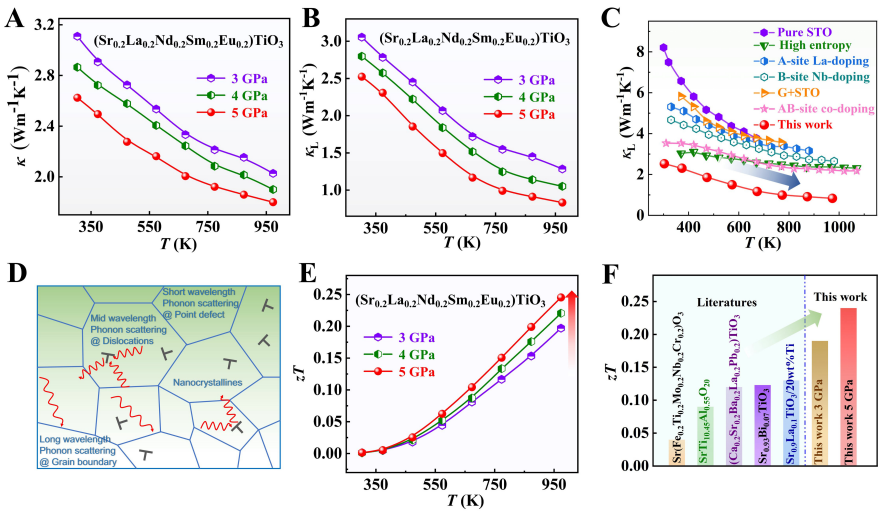

Figure 5. (A) Thermal conductivity (κ); (B) lattice thermal conductivity (κ_L) and (E) the figure of merit (zT) as a function of temperature for the 3 GPa, 4 GPa, and 5 GPa samples; (D) Schematic diagram illustrating potential phonon scattering mechanisms for reducing lattice thermal conductivity; The comparison of (C) κ_L and (F) zT values between this work and literature data.

Figure 5A illustrates the κ as a function of temperature for all $(Sr_{0.2}La_{0.2}Nd_{0.2}Sm_{0.2}Eu_{0.2})TiO_3$ ceramics under varying synthesis pressures. It is evident that κ decreases with increasing temperature for all samples. Notably, with higher synthesis pressure, the κ consistently diminishes in the whole temperature range. For example, the room-temperature κ drops from 3.1 $Wm^{-1}K^{-1}$ for the 3 GPa sample to 2.6 $Wm^{-1}K^{-1}$ for the 5 GPa sample. Especially, the lowest κ of 1.91 $Wm^{-1}K^{-1}$ at 973 K was obtained for the 5 GPa sample, which is five times lower than that of the single-crystal $SrTiO_3$[28]. Since κ is the sum of electronic κ (κ_e) and κ_L, it is important to identify the factor responsible for the substantial reduction in total κ. According to the Wiedemann-Franz equation $\kappa_e = L\sigma T$, where L is the Lorenz constant estimated using the SPB model[64], κ_e increases with σ, which rises with synthetic pressure [Supplementary Figure 5].

The κ_L is obtained by subtracting κ_e from the total κ and also shows a decreasing trend with increasing temperature [Figure 5B]. Additionally, the κ_L decreases with increasing synthesis pressure. For instance, at room temperature, the κ_L gradually declines from 3.1 $Wm^{-1}K^{-1}$ for the 3 GPa sample to 2.8 $Wm^{-1}K^{-1}$ for the 4 GPa sample and further to 2.5 $Wm^{-1}K^{-1}$ for the 5 GPa sample. Remarkably, the lowest κ_L of 0.8 $Wm^{-1}K^{-1}$ at 973 K is attained for the 5 GPa sample, which is 11 times lower than that of the single-crystal $SrTiO_3$[28], and represents the lowest κ_L reported in the literature [Figure 5C][25,28,30-32,71]. This significant reduction is ascribed to the microstructure modifications induced by high pressure. More precisely, the formation of dense point defects, dislocations, lattice distortions and nanocrystalline through high-pressure sintering significantly enhances phonon scattering over a broad wavelength range. This enhanced scattering is reflected in the scattering diagram [Figure 5D]. This work confirms that high-pressure synthesis is a feasible and effective pathway to minimizing the κ_L.

The observed increase in the PF, coupled with the reduced κ, leads to a significant improvement in the zT. As illustrated in Figure 5E, high synthesis pressure substantially enhances the zT across the entire temperature range. It is noteworthy that the 5 GPa sample achieves a maximum zT of 0.25 at 973 K, representing a 31.6% improvement compared to the 3 GPa sample. Importantly, this value is approximately 5.3 times higher than that of the original $SrTiO_3$ sample and ranks among the highest reported values for $SrTiO_3$-based materials [Figure 5F][52,70,72-74]. The substantial zT enhancement originates from two primary factors. First, pressure-induced modifications to the band structure led to an increase in n_H and m^*, while a

reduced E_{def} helps maintain a decent μ_H, thereby substantially improving the PF. Second, the high-pressure-induced formation of multiscale microstructures facilitates broad-wavelength phonon scattering, thereby leading to the minimized κ_L. This work underscores the pivotal role of high-pressure synthesis in adeptly manipulating both the band structure and microstructure, enabling substantial advancements in TE performance, particularly in oxide materials.

CONCLUSIONS

In summary, we successfully prepared the high-entropy $(Sr_{0.2}La_{0.2}Nd_{0.2}Sm_{0.2}Eu_{0.2})TiO_3$ ceramics using the high-pressure synthesis technology, and systematically examined the impact of synthesis pressure on the electrical and thermal transport properties. Our findings demonstrate that high-pressure synthesis enhances the solubility limit of rare earth elements and reduces the E_g, resulting in markedly increased n_H and an improved density-of-state effective mass. This modification effectively enhances the σ with only a minor reduction in the α, thereby improving the PF. Additionally, high-pressure synthesis induces a range of microstructural defects, including point defects, dislocations, lattice distortions, and nanoscale grains. These features collectively strengthen phonon scattering across a broad wavelength spectrum and minimize the κ_L. Consequently, an optimal zT value of 0.25 at 973 K is achieved in the $(Sr_{0.2}La_{0.2}Nd_{0.2}Sm_{0.2}Eu_{0.2})TiO_3$ sample synthesized at 5 GPa, representing a 5.3-fold improvement compared to the undoped $SrTiO_3$. This work underscores the potential of high-pressure synthesis for synergistically optimizing the carrier and phonon transport through the modulation of both E_g and microstructure, providing valuable insights for advancing TE performance.

DECLARATIONS

Authors' contributions

Design: Ma, H.; Hu, L.
Experiments and data collection: Li, X.; Luo, X.; Wang, M.; Lyu, T.
Data analysis: Li, X.; Zhang, C.; Liu, F.
Manuscript writing: Li, X.; Hu, L.
Manuscript revision and supervision: Ma, H.; Hu, L.
All authors have read and approved the final manuscript.

Availability of data and materials

The raw data supporting the findings of this study are available within this Article and its Supplementary Materials. Further data is available from the corresponding authors upon reasonable request.

Financial support and sponsorship

The work is supported by the National Natural Science Foundation of China (52471233 and 52071218), the Shenzhen Science and Technology Innovation Commission (JCYJ20230808105700001), and the Shenzhen University 2035 Program for Excellent Research (00000218). The authors also appreciate the Instrumental Analysis Center of Shenzhen University.

Conflicts of interest

All authors declared that there are no conflicts of interest.

Ethical approval and consent to participate

Not applicable.

Consent for publication

Not applicable.

REFERENCES

1. Shi, X. L.; Zou, J.; Chen, Z. G. Advanced thermoelectric design: from materials and structures to devices. *Chem. Rev.* **2020**, *120*, 7399-515. DOI PubMed
2. He, J.; Tritt, T. M. Advances in thermoelectric materials research: looking back and moving forward. *Science* **2017**, *357*, eaak9997. DOI PubMed
3. Zhu, T.; Liu, Y.; Fu, C.; Heremans, J. P.; Snyder, J. G.; Zhao, X. Compromise and synergy in high-efficiency thermoelectric materials. *Adv. Mater.* **2017**, 29. DOI
4. Wu, Y.; Nan, P.; Chen, Z.; et al. Thermoelectric enhancements in PbTe alloys due to dislocation-induced strains and converged bands. *Adv. Sci.* **2020**, *7*, 1902628. DOI
5. Tan, G.; Zhao, L. D.; Kanatzidis, M. G. Rationally designing high-performance bulk thermoelectric materials. *Chem. Rev.* **2016**, *116*, 12123-49. DOI PubMed
6. Xiao, Y.; Xu, L.; Hong, T.; et al. Ultrahigh carrier mobility contributes to remarkably enhanced thermoelectric performance in n-type PbSe. *Energy. Environ. Sci.* **2022**, *15*, 346-55. DOI
7. Li, J.; Zhang, X.; Chen, Z.; et al. Low-symmetry rhombohedral GeTe thermoelectrics. *Joule* **2018**, *2*, 976-87. DOI
8. Li, M.; Sun, Q.; Xu, S. D.; et al. Optimizing electronic quality factor toward high-performance $Ge_{1-x-y}Ta_xSb_yTe$ thermoelectrics: the role of transition metal doping. *Adv. Mater.* **2021**, *33*, e2102575. DOI
9. Wang, M.; Hong, M.; Fang, X.; et al. Engineering the p-n switch: mastering intrinsic point defects in Sb_2Te_3-dominant alloys. *Acta. Mater.* **2024**, *266*, 119675. DOI
10. Zhong, J.; Yang, X.; Lyu, T.; et al. Nuanced dilute doping strategy enables high-performance GeTe thermoelectrics. *Sci. Bull.* **2024**, *69*, 1037-49. DOI
11. Zhou, Y.; Cheng, J.; Hong, M.; et al. Orchestrating phase transition in GeTe thermoelectrics: an investigation into the role of electronegativity. *Nano. Energy.* **2024**, *127*, 109723. DOI
12. Yao, W.; Zhang, Y.; Lyu, T.; et al. Two-step phase manipulation by tailoring chemical bonds results in high-performance GeSe thermoelectrics. *Innovation* **2023**, *4*, 100522. DOI PubMed PMC
13. Huang, Y.; Lyu, T.; Zeng, M.; et al. Manipulation of metavalent bonding to stabilize metastable phase: a strategy for enhancing *zT* in GeSe. *Interdiscip. Mater.* **2024**, *3*, 607-20. DOI
14. Hu, L.; Duan, B.; Lyu, T.; et al. *In situ* design of high-performance dual-phase GeSe thermoelectrics by tailoring chemical bonds. *Adv. Funct. Mater.* **2023**, *33*, 2214854. DOI
15. Li, Y.; Liu, Y.; Wang, M.; et al. Leveraging crystal symmetry for thermoelectric performance optimization in cubic GeSe. *Rare. Met.* **2024**, *43*, 5332-45. DOI
16. Pan, L.; Liu, W.; Zhang, J.; et al. Synergistic effect approaching record-high figure of merit in the shear exfoliated n-type $Bi_2O_{2-2x}Te_{2x}$ Se. *Nano. Energy.* **2020**, *69*, 104394. DOI
17. Pei, Y. L.; Wu, H.; Wu, D.; Zheng, F.; He, J. High thermoelectric performance realized in a BiCuSeO system by improving carrier mobility through 3D modulation doping. *J. Am. Chem. Soc.* **2014**, *136*, 13902-8. DOI
18. Butt, S.; Xu, W.; Farooq, M. U.; et al. Enhancement of thermoelectric performance in hierarchical mesoscopic oxide composites of $Ca_3Co_4O_9$ and $La_{0.8}Sr_{0.2}CoO_3$. *J. Am. Ceram. Soc.* **2015**, *98*, 1230-5. DOI
19. Wang, D.; Chen, L.; Yao, Q.; Li, J. High-temperature thermoelectric properties of $Ca_3Co_4O_{9+\delta}$ with Eu substitution. *Solid. State. Commun.* **2004**, *129*, 615-8. DOI
20. Wang, Y.; Sui, Y.; Fan, H.; et al. High temperature thermoelectric response of electron-doped $CaMnO_3$. *Chem. Mater.* **2009**, *21*, 4653-60. DOI
21. Lan, J.; Lin, Y.; Liu, Y.; Xu, S.; Nan, C.; Hopper, M. High thermoelectric performance of nanostructured In_2O_3□based ceramics. *J. Am. Ceram. Soc.* **2012**, *95*, 2465-9. DOI
22. Sun, J.; Singh, D. J. Thermoelectric properties of *n*-type $SrTiO_3$. *APL. Mater.* **2016**, *4*, 104803. DOI
23. Han, J.; Zeng, Y.; Song, Y.; Liu, H. Synthesis of $SrTiO_3$ fibers and their effects on the thermoelectric properties of $La_{0.1}Dy_{0.1}Sr_{0.75}TiO_3$ ceramics. *Electron. Mater. Lett.* **2019**, *15*, 278-86. DOI
24. Lin, J.; Hwang, C.; Sie, F. Preparation and thermoelectric properties of Nd and Dy co-doped $SrTiO_3$ bulk materials. *Mater. Res. Bull.* **2020**, *122*, 110650. DOI
25. Wang, J.; Zhang, B.; Kang, H.; et al. Record high thermoelectric performance in bulk $SrTiO_3$ via nano-scale modulation doping. *Nano. Energy.* **2017**, *35*, 387-95. DOI
26. Ohta, S.; Nomura, T.; Ohta, H.; Koumoto, K. High-temperature carrier transport and thermoelectric properties of heavily La- or Nb-doped $SrTiO_3$ single crystals. *J. Appl. Phys.* **2005**, *97*, 034106. DOI

27. Ohta, H.; Kim, S.; Mune, Y.; et al. Giant thermoelectric seebeck coefficient of a two-dimensional electron gas in $SrTiO_3$. *Nat. Mater.* **2007**, *6*, 129-34. DOI
28. Rahman, J. U.; Nam, W. H.; Van, D. N.; et al. Oxygen vacancy revived phonon-glass electron-crystal in $SrTiO_3$. *J. Eur. Ceram. Soc.* **2019**, *39*, 358-65. DOI
29. Du, Y.; Zhang, M.; Wu, J.; et al. Optical properties of $SrTiO_3$ thin films by pulsed laser deposition. *Appl. Phys. A.* **2003**, *76*, 1105-8. DOI
30. Zhu, Y.; Azough, F.; Liu, X.; et al. Precursor-led grain boundary engineering for superior thermoelectric performance in niobium strontium titanate. *ACS. Appl. Mater. Interfaces.* **2023**, *15*, 13097-107. DOI
31. Zhang, B.; Wang, J.; Zou, T.; et al. High thermoelectric performance of Nb-doped $SrTiO_3$ bulk materials with different doping levels. *J. Mater. Chem. C.* **2015**, *3*, 11406-11. DOI
32. Zhang, P.; Gong, L.; Lou, Z.; et al. Reduced lattice thermal conductivity of perovskite-type high-entropy $(Ca_{0.25}Sr_{0.25}Ba_{0.25}RE_{0.25})TiO_3$ ceramics by phonon engineering for thermoelectric applications. *J. Alloys. Compd.* **2022**, *898*, 162858. DOI
33. Mizoguchi, T.; Ohta, H.; Lee, H.; Takahashi, N.; Ikuhara, Y. Controlling interface intermixing and properties of $SrTiO_3$-based superlattices. *Adv. Funct. Mater.* **2011**, *21*, 2258-63. DOI
34. Wang, Q.; Safdar, M.; Wang, Z.; He, J. Low-dimensional Te-based nanostructures. *Adv. Mater.* **2013**, *25*, 3915-21. DOI
35. Park, D.; Ju, H.; Kim, J. One-pot fabrication of Ag-$SrTiO_3$ nanocomposite and its enhanced thermoelectric properties. *Ceram. Int.* **2019**, *45*, 16969-75. DOI
36. Chen, Y.; Liu, J.; Li, Y.; et al. Enhancement of thermoelectric performance of $Sr_{1-x}Ti_{0.8}Nb_{0.2}O_3$ ceramics by introducing Sr vacancies. *J. Electron. Mater.* **2019**, *48*, 1147-52. DOI
37. Wang, Z.; Wang, Z.; Zhao, H.; et al. Behavior of boron and nitrogen impurities in diamonds synthesized at high pressure and high temperature. *Int. J. Refract. Met. Hard. Mater.* **2024**, *125*, 106902. DOI
38. Zhao, B.; You, C.; Zhang, S.; et al. Constructing coherent/semi-coherent phase boundaries to enhance toughness of superhard cBN-B composite. *IInt. J. Refract. Met. Hard. Mater.* **2024**, *123*, 106785. DOI
39. Xiao, G.; Cao, Y.; Qi, G.; et al. Pressure effects on structure and optical properties in cesium lead bromide perovskite nanocrystals. *J. Am. Chem. Soc.* **2017**, *139*, 10087-94. DOI
40. Shang, Y.; Liu, Z.; Dong, J.; et al. Ultrahard bulk amorphous carbon from collapsed fullerene. *Nature* **2021**, *599*, 599-604. DOI
41. Lyu, T.; Yang, Q.; Li, Z.; et al. High pressure drives microstructure modification and zT enhancement in bismuth telluride-based alloys. *ACS. Appl. Mater. Interfaces.* **2023**, *15*, 19250-7. DOI
42. Zhang, L.; Wang, Y.; Lv, J.; Ma, Y. Materials discovery at high pressures. *Nat. Rev. Mater.* **2017**, *2*, 1-16. DOI
43. Ninet, S.; Datchi, F.; Dumas, P.; et al. Experimental and theoretical evidence for an ionic crystal of ammonia at high pressure. *Phys. Rev. B.* **2014**, 89. DOI
44. Morozova, N. V.; Korobeinikov, I. V.; Ovsyannikov, S. V. Strategies and challenges of high-pressure methods applied to thermoelectric materials. *J. Appl. Phys.* **2019**, *125*, 220901. DOI
45. Escobedo, J.; Field, D.; Leblanc, M.; Florando, J.; Lassila, D. Influence of pressure on the microstructural evolution of Ta during shear deformation. *Scripta. Mater.* **2014**, *80*, 21-4. DOI
46. Guo, X.; Dong, H.; Luo, Z.; Chen, B.; Li, X. High pressure suppressing grain boundary migration in a nanograined nickel. *Scripta. Mater.* **2022**, *214*, 114656. DOI
47. Yin, Z.; Liu, Z.; Yu, Y.; et al. Synergistically optimized electron and phonon transport of polycrystalline BiCuSeO via Pb and Yb Co-doping. *ACS. Appl. Mater. Interfaces.* **2021**, *13*, 57638-45. DOI
48. Liu, H.; Ma, H.; Su, T.; et al. High-thermoelectric performance of TiO_{2-x} fabricated under high pressure at high temperatures. *J. Materiomics.* **2017**, *3*, 286-92. DOI
49. Wang, D.; Gao, Y.; You, C.; et al. Enhancement of thermoelectric performance in robust ZnO□based composite ceramics driven by a stepwise optimization strategy. *Adv. Funct. Mater.* **2024**, *34*, 2308970. DOI
50. Zhang, P.; Lou, Z.; Hu, G.; et al. *In-situ* construction of all-scale hierarchical microstructure and thermoelectric properties of $(Sr_{0.25}Ca_{0.25}Ba_{0.25}La_{0.25})TiO_3$/Pb@Bi composite oxide ceramics. *J. Materiomics.* **2023**, *9*, 661-72. DOI
51. Qin, M.; Lou, Z.; Zhang, P.; et al. Enhancement of thermoelectric performance of $Sr_{0.9}La_{0.1}TiO_3$-based ceramics regulated by nanostructures. *ACS. Appl. Mater. Interfaces.* **2020**, *12*, 53899-909. DOI
52. Qin, M.; Gao, F.; Wang, M.; Zhang, C.; Zhang, Q.; Wang, L. Fabrication and high-temperature thermoelectric properties of Ti-doped $Sr_{0.9}La_{0.1}TiO_3$ ceramics. *Ceram. Int.* **2016**, *42*, 16644-9. DOI
53. Koumoto, K.; Wang, Y.; Zhang, R.; Kosuga, A.; Funahashi, R. Oxide thermoelectric materials: a nanostructuring approach. *Annu. Rev. Mater. Res.* **2010**, *40*, 363-94. DOI
54. Ovsyannikov, S. V.; Shchennikov, V. V. High-pressure routes in the thermoelectricity or how one can improve a performance of thermoelectrics. *Chem. Mater.* **2010**, *22*, 635-47. DOI
55. Li, H.; Zhu, X.; Zhang, Y.; et al. Thermal conductivity and mechanical properties of as-cast and as-extruded Mg-Zn-Mn alloys. *Mat. Res.* **2019**, *22*, e20190430. DOI
56. Rodrigues, J. E. F. S.; Gainza, J.; Serrano-Sánchez, F.; et al. Unveiling the structural behavior under pressure of filled $M_{0.5}Co_4Sb_{12}$ (M = K, Sr, La, Ce, and Yb) thermoelectric skutterudites. *Inorg. Chem.* **2021**, *60*, 7413-21. DOI
57. Bueno, V. R.; Zavanelli, D.; Jung, C.; et al. Grain boundary phases in NbFeSb half□heusler alloys: a new avenue to tune transport properties of thermoelectric materials. *Adv. Energy. Mater.* **2023**, *13*, 2204321. DOI

58. Hammons, J. A.; Espitia, J. A.; Ramos, E.; et al. Pore and grain chemistry during sintering of garnet-type $Li_{6.4}La_3Zr_{1.4}Ta_{0.6}O_{12}$ solid-state electrolytes. *J. Mater. Chem. A.* **2022**, *10*, 9080-90. DOI
59. Guan, S.; Lin, W.; Liang, H.; et al. The effect of pressure tuning on the structure and mechanical properties of high-entropy carbides. *Scripta. Mater.* **2022**, *216*, 114755. DOI
60. Hu, C.; Xia, K.; Fu, C.; Zhao, X.; Zhu, T. Carrier grain boundary scattering in thermoelectric materials. *Energy. Environ. Sci.* **2022**, *15*, 1406-22. DOI
61. Qin, X.; Liu, X.; Huang, W.; Bettinelli, M.; Liu, X. Lanthanide-activated phosphors based on 4f-5d optical transitions: theoretical and experimental aspects. *Chem. Rev.* **2017**, *117*, 4488-527. DOI
62. Liang, G.; Lyu, T.; Hu, L.; et al. $(GeTe)_{1-x}(AgSnSe_2)_x$: strong atomic disorder-induced high thermoelectric performance near the ioffe-regel limit. *ACS. Appl. Mater. Interfaces.* **2021**, *13*, 47081-9. DOI
63. Zhong, J.; Liang, G.; Cheng, J.; et al. Entropy engineering enhances the thermoelectric performance and microhardness of $(GeTe)_{1-x}(AgSb_{0.5}Bi_{0.5}Te_2)_x$. *Sci. China. Mater.* **2023**, *66*, 696-706. DOI
64. Zhang, X.; Pei, Y. Manipulation of charge transport in thermoelectrics. *npj. Quant. Mater.* **2017**, *2*, 71. DOI
65. Li, J.; Zhang, X.; Lin, S.; Chen, Z.; Pei, Y. Realizing the high thermoelectric performance of GeTe by Sb-doping and Se-alloying. *Chem. Mater.* **2017**, *29*, 605-11. DOI
66. Tritt, T. M.; Subramanian, M. A. Thermoelectric materials, phenomena, and applications: a bird's eye view. *MRS. Bull.* **2006**, *31*, 188-98. DOI
67. Snyder, G. J.; Snyder, A. H.; Wood, M.; Gurunathan, R.; Snyder, B. H.; Niu, C. Weighted mobility. *Adv. Mater.* **2020**, *32*, e2001537. DOI PubMed
68. Liu, Y.; Zhao, L. D.; Liu, Y.; et al. Remarkable enhancement in thermoelectric performance of BiCuSeO by Cu deficiencies. *J. Am. Chem. Soc.* **2011**, *133*, 20112-5. DOI
69. Liu, Y.; Lin, Y.; Shi, Z.; Nan, C.; Shen, Z. Preparation of $Ca_3Co_4O_9$ and improvement of its thermoelectric properties by spark plasma sintering. *J. Am. Ceram. Soc.* **2005**, *88*, 1337-40. DOI
70. Zhang, P.; Lou, Z.; Qin, M.; et al. High-entropy $(Ca_{0.2}Sr_{0.2}Ba_{0.2}La_{0.2}Pb_{0.2})TiO_3$ perovskite ceramics with a-site short-range disorder for thermoelectric applications. *J. Mater. Sci. Technol.* **2022**, *97*, 182-9. DOI
71. Feng, X.; Fan, Y.; Nomura, N.; et al. Graphene promoted oxygen vacancies in perovskite for enhanced thermoelectric properties. *Carbon* **2017**, *112*, 169-76. DOI
72. Banerjee, R.; Chatterjee, S.; Ranjan, M.; et al. High-entropy perovskites: an emergent class of oxide thermoelectrics with ultralow thermal conductivity. *ACS. Sustainable. Chem. Eng.* **2020**, *8*, 17022-32. DOI
73. Li, Y.; Yamamoto, S.; Ahmad, K.; Almutairi, Z.; Koumoto, K.; Wan, C. Localized vibration and avoided crossing in $SrTi_{11}O_{20}$ for oxide thermoelectrics with intrinsically low thermal conductivity. *J. Mater. Chem. A.* **2021**, *9*, 11674-82. DOI
74. Chen, C.; Bousnina, M.; Giovannelli, F.; Delorme, F. Influence of Bi on the thermoelectric properties of $SrTiO_{3-\delta}$. *J. Materiomics.* **2019**, *5*, 88-93. DOI